

Charged impurity-induced scatterings in chemical vapor deposited graphene

Ming-Yang Li, Chiu-Chun Tang, D. C. Ling, L. J. Li, C. C. Chi, and Jeng-Chung Chen

Citation: [Journal of Applied Physics](#) **114**, 233703 (2013); doi: 10.1063/1.4852435

View online: <http://dx.doi.org/10.1063/1.4852435>

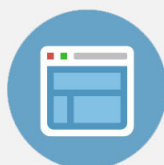
View Table of Contents: <http://scitation.aip.org/content/aip/journal/jap/114/23?ver=pdfcov>

Published by the [AIP Publishing](#)

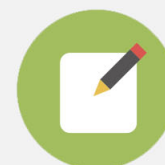


Re-register for Table of Content Alerts

Create a profile.



Sign up today!



Charged impurity-induced scatterings in chemical vapor deposited graphene

Ming-Yang Li,¹ Chiu-Chun Tang,¹ D. C. Ling,² L. J. Li,^{1,3} C. C. Chi,^{1,4}
 and Jeng-Chung Chen^{1,4}

¹Department of Physics, National Tsing Hua University, Hsinchu 30013, Taiwan

²Department of Physics, Tamkang University, Tamsui Dist., New Taipei 25137, Taiwan

³Institute of Atomic and Molecular Sciences, Academia Sinica, Taipei 11529, Taiwan

⁴Frontier Research Center on Fundamental and Applied Sciences of Matters, National Tsing Hua University, Hsinchu 30013, Taiwan

(Received 13 September 2013; accepted 6 December 2013; published online 20 December 2013)

We investigate the effects of defect scatterings on the electric transport properties of chemical vapor deposited (CVD) graphene by measuring the carrier density dependence of the magneto-conductivity. To clarify the dominant scattering mechanism, we perform extensive measurements on large-area samples with different mobility to exclude the edge effect. We analyze our data with the major scattering mechanisms such as short-range static scatters, short-range screened Coulomb disorders, and weak-localization (WL). We establish that the charged impurities are the predominant scatters because there is a strong correlation between the mobility and the charge impurity density. Near the charge neutral point (CNP), the electron-hole puddles that are induced by the charged impurities enhance the inter-valley scattering, which is favorable for WL observations. Away from the CNP, the charged-impurity-induced scattering is weak because of the effective screening by the charge carriers. As a result, the local static structural defects govern the charge transport. Our findings provide compelling evidence for understanding the scattering mechanisms in graphene and pave the way for the improvement of fabrication techniques to achieve high-quality CVD graphene. © 2013 AIP Publishing LLC. [<http://dx.doi.org/10.1063/1.4852435>]

I. INTRODUCTION

Graphene is a single layer of sp^2 -bonded carbon atoms with a honeycomb lattice structure. The unique crystal structure of graphene leads to an intriguing band structure: a linear and chiral dispersion relation with a four-fold ground state degeneracy that accounts for both spin and valley.¹ The fascinating electronic and optic properties of graphene have attracted intense scientific interests and technological efforts since the discovery of graphene.^{2–4} However, to further commercialize graphene-based devices, two primary obstacles in the material preparation must be overcome. First, for the widespread applications of graphene, it is essential to have reliable methods to produce large-scale uniform graphene with high yield. Several techniques have been developed to produce graphene using controlled growth and large areas, including epitaxial growth on SiC,^{5,6} and chemical vapor deposition (CVD).⁷ However, the large samples that are grown using these methods inevitably suffer defects and impurities during the fabrication processes. It then comes to the second issue that these disorders severely degrade the quality of graphene, which causes large variations of mobility and significant reductions in reproducibility of the device characteristics.^{8,9} To date, the role of different impurities in the deterioration of the transport properties of graphene and the method to characterize various scattering processes remain crucial issues that have not been fully addressed.

Several theories have been developed to elucidate the disorder effects in the transport properties of graphene; these theories mainly focus on the temperature, the magnetic field, and the carrier density dependences of the conductivity. One

outstanding example is the phenomenon of weak localization (WL), which is observed in magnetoconductivity (MC). WL signal is known to be a sensitive probe to investigate both the inelastic- and elastic-scattering mechanisms in materials. For ideal graphene, the chiral nature of electrons hinders the backscattering process because of the pseudospin conservation.¹⁰ Consequently, the conventional WL of two-dimensional system is suppressed whereas the weak anti-localization (WAL) becomes pronounced. However, recent studies suggest that the presence of sharp defects (atomic-range scatters) or charged impurities with a finite range can induce elastic intra- and inter-valley scattering and restore WL.^{11–13} Theoretical calculations further illustrate the effects of the charged disorders on the carrier density dependence and the temperature dependence of the conductivity and the minimum conductivity.^{14–16} It has been argued that the presence of the charged impurities can induce local potential fluctuations and form inhomogeneous electron-hole puddles near the charge neutral point (CNP). Note that the potential profile of the puddles strongly depends on the carrier density, which is essentially different from that of the static puddles that arise from the intrinsic ripples of natural graphene.

Numerous experiments have been performed to investigate the WAL and WL effects in graphene. Depending on the experimental conditions, one can observe either WL or WAL of carriers in graphene.¹⁷ It is believed that inelastic scattering is caused by the electron-electron interaction.^{18,19} The inter-valley and intra-valley scatterings are attributed to the boundary effect of a small sample, the structural defects, and the warping effect.^{18–20} As yet, the questions regarding

what the dominated scatter is remain unanswered.^{18,20–22} Earlier studies mainly rely on exfoliated graphene, which typically has high mobility but is small size (less than $5\ \mu\text{m}$).^{17–20} To eliminate the boundary scattering, it is desirable to measure MC in larger samples. Moreover, the scattering effects that are induced by the charged disorders are sensitive to the carrier density, whereas those induced by the structural defects are not. Thus, it is informative to study the evolutions of MC in samples with different carrier densities to distinguish the roles of different types of scatters.

In this work, we attempted to explore the disorder-induced scattering processes in large-area CVD-grown graphene. We measured the carrier density dependence of the MC that crosses the CNP using several samples with different qualities. To properly interpret the observed WL signals, the effects of the charged impurity were considered. Based on the theoretical models, the characteristic times that are associated with different scattering processes, the charged impurity density, and the averaged amplitude of the scattering potential were extracted. An empirical relationship between the mobility and the charged impurity density was established. Our experimental findings suggest that the electron-hole puddles, which are induced by the charged impurities, play a dominant role in the electronic transport of the graphene under examination, particularly in the vicinity of the charge neutral point.

II. SAMPLE CHARACTERIZATIONS

A large-area graphene sheet was grown using CVD on a Cu foil. Subsequently, it was dissolved in an $\text{Fe}(\text{NO})_3$ solvent and transferred onto a clean SiO_2 ($\sim 300\text{ nm}$)/p-Si substrate. The detailed growth parameters and the transfer procedures have been published elsewhere.²³ After the transfer, graphene was patterned into a Hall-bar geometry using photolithography and O_2 plasma etching. Finally, $16\text{ nm}/4\text{ nm}$ thick of Au/Cr metal contacts were deposited using thermal evaporation. Table I summarizes the main characteristics of five samples. The results presented in this

TABLE I. Specifications of the samples studied in the experiments. All samples were patterned into Hall-bar geometry. Here, W denotes the width of the device, and L is the separation between the voltage probes of the Hall-bar device. The carrier density n_0 is determined from the Hall coefficient at $V_g \sim 0\text{ V}$, and μ is the electron mobility estimated at $T = 10\text{ K}$. The parameters n_i , n^* , and V_{rms} are extracted from the best curve fitting to theoretical models that are described in the text, where n_i represents the charged impurity density, n^* is the density of electron-hole puddle, and V_{rms} is the standard deviation of the potential fluctuation.

Sample	S1	S2	S3	S4	S5
$W\ \mu\text{m}$	10	10	10	10	5
$L\ \mu\text{m}$	20	20	20	20	30
$n_0 \times 10^{12}\text{ cm}^{-2}$	1.01	3.23	2.3	2.1	1.02
$\mu\text{ cm}^2/\text{Vs}$	3600	930	1300	1800	3300
$n_i \times 10^{12}\text{ cm}^{-2}$	1.4	7.0	5.1	4.3	1.9
$n^* \times 10^{11}\text{ cm}^{-2}$	3.8	19	15	12	5.5
$V_{rms}\text{ meV}$	106	185	164	155	114

work are primarily obtained from samples S1 and S2, which have the highest and the lowest mobilities with different extents of disorders among the investigated samples.

Micro-Raman spectroscopy was performed at a 473 nm laser excitation with a spatial resolution of $0.6\ \mu\text{m}$ to characterize the structural quality, the homogeneity, and the layer number of the CVD graphene that was transferred onto the SiO_2/Si substrate. Figure 1(a) shows the Raman spectra of samples S1 and S2 with the intensity ratio of 2D to G peaks (I_{2D}/I_G) larger than two. The tiny D peak $\sim 1350\text{ cm}^{-1}$, which is indicative of structural defects, were found in both S1 and S2.^{24,25} Figure 1(b) illustrates a spatial Raman map of I_{2D}/I_G with a step resolution of $1\ \mu\text{m}$ for S2; 92% of the area of the sample exhibits $I_{2D}/I_G > 2$, which suggests a high uniformity of the monolayer graphene.²⁴ To make a rough estimation of the spatial distribution of structural disorders, we measured the spatial mapping of I_D/I_G , as shown in Fig. 1(c). Figure 1(d) shows a histogram of the I_D/I_G ratio of samples S1 (white) and S2 (black). Comparing with the optical images, we can identify that the pronounced D peak ($I_D/I_G > 0.7$) may be caused by dusts or resistant residue on the studied graphene. If we take the histogram of $I_D/I_G > 0.2$ as a signature of the presence of structural defects, which usually behave as local sharp scatters, the structural defects spread over $\sim 31\%$ of the area of samples S1 and S2. However, the fact that the two samples, which have significantly different mobilities, as listed in Table I, have approximately the same D-peak density, which strongly indicates that the structural defects may not be the dominant source responsible for mobility degradation.

Figures 2(a) and 2(b) show the four-terminal longitudinal resistance R_{xx} and the Hall coefficient R_H as a function of the back gate voltage V_g measured at a temperature $T = 10\text{ K}$ for S1 and S2, respectively. The Hall coefficient is defined as

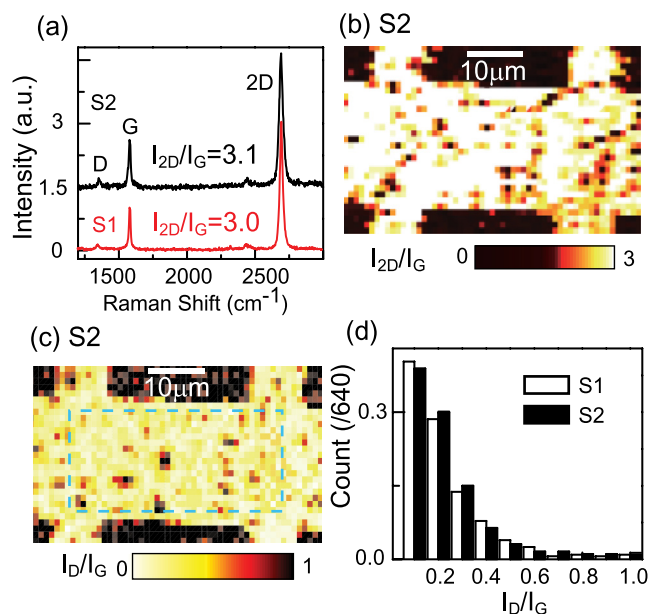


FIG. 1. (a) Raman spectrum of samples S1 and S2. The map of intensity ratio (b) I_{2D}/I_G and (c) I_D/I_G for S2. The scale bar is $10\ \mu\text{m}$. (d) The histogram of the I_D/I_G intensity counts, which was normalized with the total count for S1 (white) and S2 (black). The examined region is within the dashed box in (c).

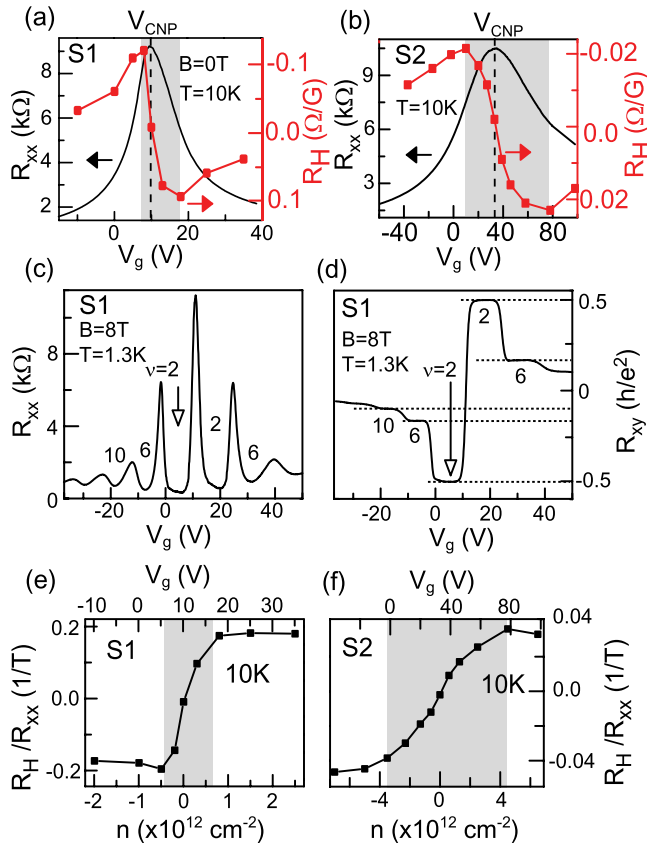


FIG. 2. (a), (b) Longitudinal resistance R_{xx} and Hall coefficient R_H versus gate voltage V_g at temperature $T = 10$ K for S1 and S2, respectively. The charge neutral point, V_{CNP} , is located at V_g of approximately 10 V for S1 and 33 V for S2. The gray area marks the transition regime of R_H . (c), (d) R_{xx} and R_{xy} of S1 as a function of V_g at magnetic field $B = 8$ T and a temperature $T = 1.3$ K. The numbers specify the filling factors $\nu = 2-10$. (e), (f) The Hall coefficient R_H that is normalized to R_{xx} as a function of the carrier concentration n for S1 and S2, respectively. The gray area marks the transition regime of R_H/R_{xx} for S1 and S2.

$R_H = R_{xy}/B$, where R_{xy} denotes the Hall resistance. Our CVD graphene is typically hole-doped, which results in a positive shift of the CNP voltage, V_{CNP} , to ~ 10 V for S1, and ~ 33 V for S2. The ambipolar behavior of the sign reversal of R_H versus V_g across V_{CNP} is properly observed. Figures 2(c) and 2(d) show R_{xx} and R_{xy} of S1 as a function of V_g at a fixed magnetic field $B = 8$ T and a temperature $T = 1.3$ K. R_{xy} exhibits well-resolved quantized plateaus at $\pm h/(2e^2)$, $\pm h/(6e^2)$, and $\pm h/(10e^2)$ for both electron- and hole-like carriers, which indicates that the superior quality of the electronic quality of our CVD graphene with a mobility of $3600 \text{ cm}^2/\text{Vs}$ is comparable with that of exfoliated graphene. Nevertheless, we note that the R_{xx} that accompanies a plateau in R_{xy} exhibits a local minimum with a finite value, which is distinctly different from the vanishing R_{xx} in clean graphene flakes that are prepared by mechanical exfoliation.²⁶ It has been reported that R_{xx} at the quantized Hall plateau is attributed to the effects of disorder-induced scatterings.²⁷

The sign change in the slope of R_H crossing V_{CNP} is resulted from the cancellation of electron and hole puddles. If the electron-hole puddles are induced by the surface roughness associated with the manifestation of the substrate morphology, the electron and hole puddles should be

comparable for both S1 and S2 samples. In contrast, the transition width of R_H , which is marked with the gray areas in Figs. 2(a) and 2(b), is much wider for the lower mobility sample of S2. Therefore, it is unlikely that the surface roughness is notably responsible for the mobility variations. A recent theory by Yan and Ting indicates that R_H/R_{xx} approaches zero at the CNP and saturates at larger n under charged impurity scatterings.²⁸ The saturation of R_H/R_{xx} implies that both the longitudinal and the transverse conductivities are proportional to the carrier concentration n , and the electric transport is governed by one type of carrier. Figures 2(e) and 2(f) show the R_H/R_{xx} as a function of n (or V_g) for S1 and S2, respectively. Here, $n = \alpha(V_g - V_{CNP})$, and a conversion ratio α is estimated to be $0.95 \times 10^{11} \text{ cm}^{-2}/\text{V}$ with a SiO_2 substrate thickness of 300 nm. The gray area denotes the transition region of R_H/R_{xx} . The general behaviors of the carrier density-dependent R_H/R_{xx} qualitatively agree well with the theoretical predictions, which suggests that the charged impurity may induce the extra electron-hole puddles and accordingly tune the transition width.

III. WEAK LOCALIZATION IN CVD GRAPHENE

In this section, we present the studies of the MC of graphene with different mobilities. Figures 3(a) and 3(b) show the representative traces of MC, $\Delta\sigma = \sigma(B) - \sigma(0)$, which were measured at different V_g and at a fixed temperature of 10 K for S1 and S2. The curves in this figure emphasize the evolution of MC from a high-carrier-density regime across the charge neutral regime. At all gate voltages, MC is positive and shows a sharp dip at low B , which represents the general features of WL. Regardless of the carrier polarity, MC exhibits reproducible fluctuations at larger B , which can be identified as a universal conductance fluctuation. Furthermore, note that the side wings of the MC traces at

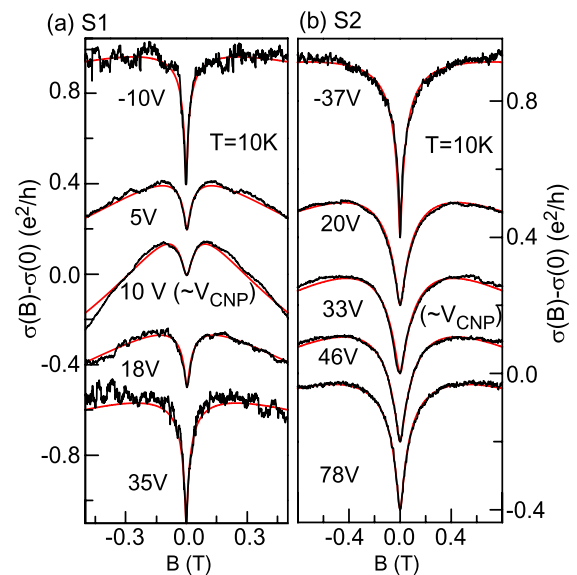


FIG. 3. Magnetoconductivity measured in (a) sample S1 and (b) sample S2. Each trace was taken at different gate voltages V_g , indicated by the number below. The curves with $V_g = -10$ V, 5 V, 18 V, and 35 V for S1 and -37 V, 20 V, 46 V, and 78 V for S2 have been shifted for clarity. The red solid lines are the best fitting curves to the theoretical model.

larger B values exhibit a distinct downturn near the CNP, which is a signature of WAL.

To further analyze the above experimental data, we adopt the WL theory developed by McCann *et al.*¹¹ and Yan *et al.*^{12,29} Reference 11 considers an atomically sharp disorder with the effect of a trigonal warping of the bands; in contrast, Ref. 12 addresses a finite-range potential induced by charged impurities. It has been shown that both approaches lead to consistent results in the limit of short scattering length.²⁹ Therefore, for simplicity, we adopt the work by McCann *et al.* to extract the relevant scattering times of the studied samples; the relevant scattering times include the inelastic scattering time τ_ϕ , the inter-valley elastic scattering time τ_i , and the intra-valley elastic scattering time τ_* from the curve fitting to the MC data. The MC correction can be expressed as

$$\frac{\pi\hbar}{e^2}(\sigma(B) - \sigma(0)) = F\left(\frac{\tau_B^{-1}}{\tau_\phi^{-1}}\right) - F\left(\frac{\tau_B^{-1}}{\tau_\phi^{-1} + 2\tau_i^{-1}}\right) - 2F\left(\frac{\tau_B^{-1}}{\tau_\phi^{-1} + \tau_i^{-1} + \tau_*^{-1}}\right), \quad (1)$$

where $F(z) = \ln(z) + \psi(0.5 + z^{-1})$, $\psi(x)$ is a digamma function, $\tau_B^{-1} = 4eDB/\hbar$, $D = v_F l/2$ is the diffusion constant with $D \sim 0.02$ m²/s for S1 and 0.01 m²/s for S2, $v_F \approx 10^6$ m/s is the Fermi-velocity, and l is the mean free path.^{18,20} Obviously, a significant inter-valley scattering with small τ_i will suppress the second and the third terms on the right-hand side of Eq. (1), which will enhance WL.

By using the characteristic times τ_ϕ , τ_i and τ_* as three free parameters in curve fitting, the best fits to Eq. (1) are shown in Figs. 3(a) and 3(b) as solid red curves. Accordingly, Figures 4(a)–4(c) and 4(d)–4(f) summarize the extracted τ_ϕ , τ_i , and τ_* as a function of n for S1 and S2, respectively. The fitting errors, which are presented either as the length of the scale bar or the size of the symbols in Fig. 4, are estimated using the standard deviation of the best fits. As shown in Fig. 4, the

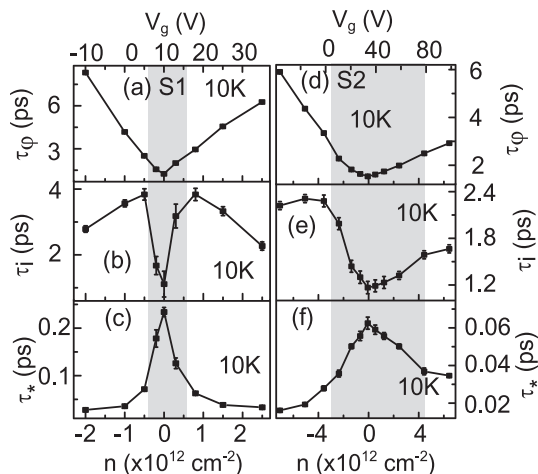


FIG. 4. Carrier density dependent characteristic times extracted from the WL theory. (a), (d) Inelastic scattering time τ_ϕ , (b), (e) inter-valley elastic scattering time τ_i , and (c), (f) intra-valley elastic scattering time τ_* as a function of n for S1 and S2, respectively. The data were obtained at $T = 10$ K. The gray area indicates the regime where τ_i drops.

sample with lower mobility has shorter characteristic scattering times. The fitting results lead to $\tau_i \leq \tau_\phi$ and $\tau_* < \tau_\phi$, which indicates a strong inter-valley scattering regime.¹³ Toward the CNP, τ_ϕ decreases whereas τ_* increases. The general behaviors of τ_ϕ and τ_* as a function of n are consistent with the earlier reports.^{18–20} The decrease of τ_ϕ with n near the CNP has been interpreted by increasing the electron-electron Nyquist interaction.¹⁹ Consequently, it causes a significant loss of phase coherence near the CNP, which manifests itself as a wider and smaller dip in the MC curve around the zero magnetic field as shown in Fig. 3. A larger τ_* can enhance the WAL behavior and may be responsible for the observed downturn of the side wings of in the MC traces at higher magnetic fields. More interestingly, τ_i displays more complicated variations with n . As n approaches the CNP, τ_i first tends to increase, and consequently drops near the CNP, as shown in Figs. 4(b) and 4(e). Note that the suppression of τ_i near the CNP, which is shown in the gray regime, has been observed in exfoliated graphene.²⁰

Despite numerous studies, a variety of WL phenomena that have been observed in graphene with different carrier densities and mobilities are not well understood.^{17–20} Earlier experiments suggest that the characteristic scatterings times are related to the warping effect in the presence of sharp disorders.^{11,18,20,21} However, the warping effect alone cannot explain the variations of the scattering times among different samples, in particular near the CNP. The extracted τ_* is much smaller than the theoretical value of τ_w , which varies from 10 ps for $n = 2 \times 10^{12}$ cm⁻² to 450 ps for $n = 3 \times 10^{11}$ cm⁻², where $\tau_w = (l/v_F)(\gamma_0 a^2 E_F^2 / 8\hbar^3 v_F^2)^2$, $\gamma_0 = 3$ eV is the nearest-neighbor coupling strength, and a is the lattice constant, which is associated with the warping effect.^{11,18} In addition, it is difficult to account for the carrier density dependence of τ_* and τ_i near the CNP merely from the scattering of atomically sharp defects.^{18,20,22}

We then turn to consider the effect of charged disorders on MC. The most distinct characteristic of the charged impurity is the variations of the scattering length with n because of the screening effects. The calculations performed by Yan *et al.* indicate that the Coulomb interaction between the charged impurities and the carriers becomes weaker as n decreases, which makes τ_* larger near the CNP.^{12,29} On the other hand, the spatial distribution and the potential fluctuation of the electron-hole puddles, which are induced by the charged impurities both increase near the CNP due to a weak screening effect. We surmise that more frequent scattering crossing electron-hole boundaries may be related to the reduction of τ_i . Therefore, the charge inhomogeneity is closely related to n and the charged impurity density, which could be sample dependent. The common feature, a characteristic gray regime marked in Figs. 2(a)/2(b), 2(e)/2(f), and 4(b)/4(e) for S1/S2, provides compelling evidence that the charged impurity plays a dominant role in the electric transport of the investigated CVD graphene.

IV. CHARGED DISORDER

To elucidate the effect of the charged impurities on the electronic transport of graphene, we adopted a semi-classical

theory developed by Das Sarma *et al.*^{13–16} The theory assumes that the charged impurities with density n_i are randomly distributed at the interface between the graphene and the substrate, which creates a local electrostatic fluctuating potential $V(r)$. The potential fluctuation can be described using a statistical distribution $P(V)$ with a Gaussian form, i.e., $P(V) = e^{-V^2/2V_{rms}^2}/\sqrt{2\pi V_{rms}^2}$, where V_{rms} is the standard deviation of the potential fluctuation.¹⁶ $V(r)$ leads to the formation of an inhomogeneous network of electron-hole puddles in graphene. Neglecting the detailed scattering processes, the charge transport that is affected by the charged impurities can be described using the average of the Boltzmann results. Within this framework, the conductance can be expressed as¹⁵

$$\sigma(n) = \begin{cases} 20 \frac{e^2}{h} \frac{n^*}{n_i} & \text{if } n < n^* \\ 20 \frac{e^2}{h} \frac{n}{n_i} & \text{if } n > n^*, \end{cases} \quad (2)$$

where n^* is the density of the electron-hole puddle and n_i is the charged impurity density. Experimentally, R_{xx} or σ^{-1} , is asymmetrical with respect to the CNP [see Figs. 2(a) and 2(b)], which suggests that the impurity dopant not only contributes to the carriers but also subtly alters the scattering processes. Because the studied graphene samples are all intrinsic p-doped, we can fit our $\sigma(n)$ data in case of $n > n^*$ to extract n_i using Eq. (2) in the hole regime. The red dotted lines in Figs. 5(a) and 5(b) show the representative fitting results for S1 and S2, respectively. After obtaining n_i , we can derive n^* from Eq. (2) in the case of $n < n^*$.

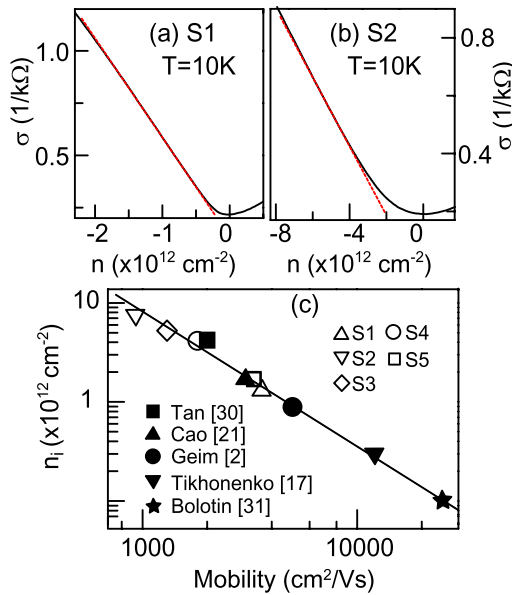


FIG. 5. (a), (b) Conductivity as a function of n for S1 and S2, respectively. The red dotted line is the theoretical fitting by Eq. (2). (c) The charged impurity density n_i versus the mobility μ (estimated at $T = 10\text{K}$) plot. The hollow symbols represent our data, and other experimental works are incorporated: exfoliated graphene, \blacksquare Tan *et al.*,³⁰ \bullet Geim and Novoselov,² \blacktriangledown Tikhonenko *et al.*,¹⁷ CVD graphene, \blacktriangle Cao *et al.*,²¹ suspended graphene, \star Bolotin *et al.*³¹ The solid line is the fitting curve with $n_i = 7.24 \times 10^4 \times \mu^{-1.32}$.

Next, we attempt to quantify V_{rms} with different n_i values in the framework of a microscopic self-consistent theory, where V_{rms} can be expressed as¹⁶

$$V_{rms}^2 = 2\pi n_i e^2 \times \int \left[\frac{2e^{-k'z_0} Z e \sinh(dk')}{k' \kappa_{ins} \cosh(dk') + (k' \kappa_v + 2q_{TF} \kappa) \sinh(dk')} \right]^2 k' dk', \quad (3)$$

where q_{TF} is the Thomas-Fermi screen wave vector, $\kappa_{ins} = 3.9$ is the dielectric constant of SiO_2 , $\kappa_v = 1$ is the dielectric constant in vacuum, $d = 300\text{nm}$ is the thickness of SiO_2 , Z is the charge number of the impurity, and z_0 is the distance of the impurity from the graphene/substrate interface. The precise value of z_0 is not crucial in the calculation because a small Fermi-energy is concerned. Therefore, we choose $z_0 = 1\text{nm}$ as a general consideration.¹⁵ The value of Z ranges from 1 to 2 because the possible source of charged impurity is either H_2O , which was absorbed at the graphene/substrate interface, or the ion residue from Cu foil etching during the transfer process. Here, we simply assume that $Z = 1$ and evaluate V_{rms} for the studied samples with n_i extracted from the curve fitting described above. The values of n_i , n^* , and V_{rms} for the studied samples are summarized in Table I. It is clear that a sample with higher n_i consistently has higher intrinsic hole carrier density, which indicates that the charged impurities are p-dopant. Note that the values of V_{rms} and n^* , which are listed in Table I, are estimated at the CNP. In general, V_{rms} and n^* vary with n because of the carrier density-dependent screening effect.

To find the correlations between the charged impurities and the sample quality, we plot the charged impurity density, n_i , versus the mobility, μ , for the studied samples and those prepared by various groups with different methods in Fig. 5(c).^{2,17,21,30,31} The hollow symbols are data obtained from the samples studied, and the solid symbols are data extracted from the earlier reports. It is remarkably interesting that n_i increases with the decreasing mobility, and all of the data follow a linear relationship in a logarithmic scale, which yields an empirical relationship of $n_i = 7.24 \times 10^4 \times \mu^{-1.32}$. This finding strongly suggests that the charged impurity is predominantly responsible for the degradation of graphene quality. We note that the values of n_i that were extracted from the electron regime in our samples are laid within the size of the symbols. It should be mentioned that the empirical relationship is different from the theoretical prediction with $n_i \propto \mu^{-1}$ based on the independent charged impurity assumption.¹⁵ The discrepancy may be attributed to presence of the correlation between the charged impurities or a less effective screening effect of the carriers in a regime with higher-impurity-density, which gives the nonlinear relation between n_i and μ^{-1} .³²

Let us address the extent to which the empirical relationship between n_i and μ is valid. It has been shown that the acoustic phonon and surface optical phonon scatterings are suppressed, and the impurity scattering dominates in graphene below 100K .³³ Earlier experimental studies further suggest that the mobility extracted away from the CNP

(to eliminate the effect induced by the electron-hole puddle) saturates at low temperatures.^{34,35} In addition, the theory that we adopted to extract n_i from Eq. (2) does not consider all phonon effects. Thus, we reasonably believe that the empirical relationship of $n_i \propto \mu^{-1.32}$ is applicable to graphene with charged impurities at temperature below 100 K. To further justify the above argument, we revisit the data for graphene prepared from reduced graphene oxide, which was reported in the literature.³⁶ This type of graphene has a large number of structural defects, and we apply Eq. (2) to deduce the relevant physical quantities. The results are as follows: $n_i = 7 \times 10^{14} \text{ cm}^{-2}$, $n^* = 7.1 \times 10^{12} \text{ cm}^{-2}$, and $V_{rms} = 770 \text{ meV}$, with $\mu = 5 \text{ cm}^2/\text{Vs}$, which clearly deviate from the above trends for graphene with charged impurities.

V. DISCUSSIONS

Our studies reveal two types of distinct disorders in CVD graphene: the structural defects and the charged impurities. The structural defects such as punctuated holes, surface corrugations, and grain boundaries usually behave as sharp short-range scatters. In contrast, the charged impurities give rise to fine-range scattering, which strongly depends on the screening effect or n . The structural defect density presented in the studied samples with $\mu \sim 1000\text{--}4000 \text{ cm}^2/\text{Vs}$ are approximately 10^{11} cm^{-2} , as identified by the Raman I_D peaks. As listed in Table I, the charged impurity density in the studied samples is one order of magnitude higher than the structural defect density. Away from the CNP, where n is high, the sharp and local structural defects are expected to be the dominant scattering source. In strong contrast, near the CNP, where n is low, the screening effect is weak and the scattering by the charged impurities can gradually become more pronounced. Consequently, the electric transport near the CNP is possibly complicated by the presence of the electron-hole puddles, which are induced by the charged impurities.

To illustrate the above scenario, we simulated the spatial potential profile V_e , which is associated with a spatial averaged value of V_{rms} . The adopted parameters are $V_{rms} = 106 \text{ meV}/185 \text{ meV}$ and $n^* = 3.8 \times 10^{11} \text{ cm}^{-2}/1.9 \times 10^{12} \text{ cm}^{-2}$ for S1/S2 at the CNP (see Table I). Figures 6(a) and 6(b) depict the intensity plot of V_e over $100 \text{ nm} \times 100 \text{ nm}$ at different E_F values for S1 and S2, respectively. The dispersed blue/red patches represent the electron/hole puddles. Figures 6(c) and 6(d) correspond to a cross-section profile of V_e for the dashed lines that cut through the V_e map, which are shown in Figs. 6(a) and 6(b). Figure 6 reveals several unique features of the charged impurity. For samples with lower μ and more n_i , the areas of the electron-hole puddles are smaller, and the spatial distributions of the puddles are denser; meanwhile, the fluctuation amplitude of V_{rms} is larger because of a weaker screening effect. These facts offer reasonable explanations why S2 has shorter scattering times of τ_i and τ^* than S1. As n increases, the charged impurities are effectively screened, and V_{rms} becomes smaller, as shown in Figs. 6(c) and 6(d). As E_F is comparable to $V_{rms}(V_{CNP})$, the electron-hole puddles almost vanish, as shown in the bottom panel of Fig. 6(a). We can assume that $E_F = \hbar v_F \sqrt{\pi n}$ and estimate that $\Delta V_g (= \pm \frac{1}{\pi n} (\frac{V_{rms}}{\hbar v_F})^2)$, as $E_F \sim V_{rms}(V_{CNP})$.

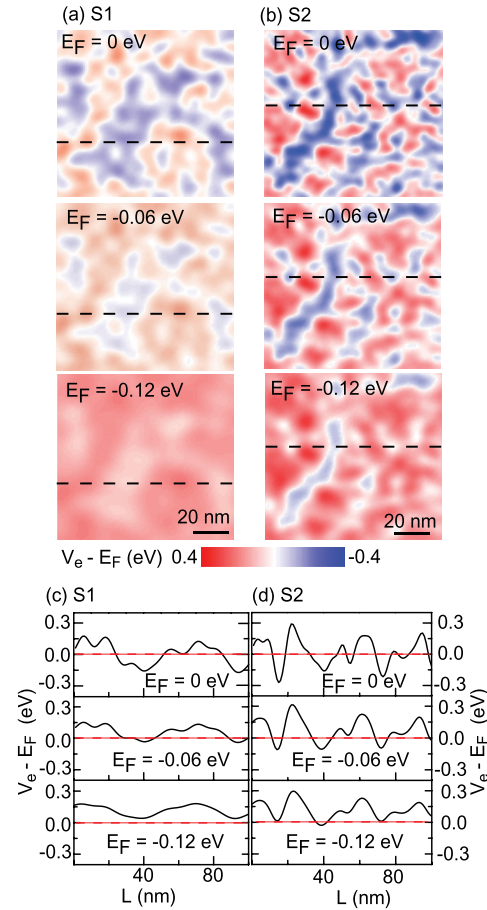


FIG. 6. (a) and (b) Potential profile for the effective potential V_e at different E_F values for S1 and S2, respectively. The scale bar for the spatial distance is 20 nm. (c), (d) The spatial distribution of the potential profile along the marked dashed line in (a) and (b) for S1 and S2, respectively. The red dashed lines indicate the energy levels that the carriers occupy.

Then, $\Delta V_g \sim \pm 6 \text{ V}$ for S1 and $\sim \pm 31 \text{ V}$ for S2, which are qualitatively in good agreement with the observed transition width that is marked in gray in Fig. 4. Note that the discrepancy between the simulated and the observed transition widths is reduced if we use $Z = 1.3$ to evaluate V_{rms} and ΔV_g for S2, which indicates that the charged impurity source in S2 may contain more ion residue with a higher valence state.

After knowing the potential profile in the presence of the charged impurities, we are now ready to identify the regime where the charged impurities govern the carrier-density-dependent scattering times of the studied samples. As $E_F \gg V_{rms}$ in the high carrier density regime, the charged impurities are effectively screened, and the sharp local structural defects become more important. The WL signal is experimentally observed and can be fitted rather well using the approach by McCann *et al.* In contrast, as $E_F \leq V_{rms}$ in the low carrier density regime, the scattering rate can be significantly enhanced by the emergence of the electron-hole puddles. Moreover, comparing with an earlier report,¹⁷ we can estimate that the charged impurity density of graphene should be on the order of 10^{11} cm^{-2} , which is one order of magnitude smaller than that of the studied samples, to observe a pronounced WAL signal.

After interpreting our observations, we wish to stress the shortcomings of the current understanding of the disorder effects. First, a detailed examination of our $\sigma(V_g)$ traces and many earlier reports shows a common feature that $\sigma(V_g)$ is asymmetrical with respect to V_{CNP} , even at large n . This common feature suggests that the charged impurities not only behave as a dopant, but also profoundly break the electron-hole symmetry in the scattering processes. The asymmetry of $\sigma(V_g)$ has been addressed in terms of the potential difference between the metal contact and the doped graphene channel for two-terminal devices.³⁷ However, this argument is no longer valid for four-probe measurements. A comprehensive understanding of the underlying scattering mechanism can elucidate the nature of the impurity, and pave the way for graphene-based device applications. Second, the current theories commonly assume that there is no correlation among the impurities, which may only be valid away from the CNP. The recent experiments show that the inter-impurity correlations should be considered at low n .^{38,39} Third, larger fitting discrepancies based on the WL theory are consistently found near the CNP. To have a better quantitative analysis, the presence of the electron-hole puddles should be specifically included in the magnetoconductance correction.

In summary, we have extensively investigated the longitudinal resistance, the Hall coefficient, and the magnetoconductivity as a function of the carrier density for large-area CVD graphene with different mobilities. The characteristic scattering times are extracted from the WL analysis. We find that the slope change of the Hall coefficient R_H , the evolution of R_{xx}/R_H away from a saturation trend, and the reduction of the inter-valley scattering time coincidentally fall within a low carrier density regime, where the transition width is wider for lower mobility samples. All of these features can be understood by considering the charged impurity induced scatterings. We deduce a strong correlation between the mobility μ and the charged impurity density n_i and conclude that the charged impurities are the predominant scatters for the electric transport of the studied CVD graphene. Then, we illustrate the change of the charged-impurity-induced scattering potential with the carrier density n . When n is high, the charged impurity induced scattering is weak because of a strong screening by the charge carriers. Accordingly, the scattering process by the local structural and sharp defects is dominated. In contrast, when n is low, the charged impurities are less screened and can induce the electron-hole puddles with density and the associated potential fluctuation depending on n_i and n . Therefore, the presence of the electron-hole puddles determines the minimum conductivity. Our experimental findings suggest that removing the charged impurities is decisively important for fabricating reproducible high-quality CVD graphene for potential device applications.

ACKNOWLEDGMENTS

We acknowledge Chung-Yu Mo, C. S. Ting, and Xin-Zhong Yan for helpful discussions and Ang-Yu Lu and J. Y. Juang for assistance with the experiments. This work was supported by the Department of Natural Science at the

National Science Council under Grant No. NSC 101-2628-M-007-002-MY3, Taiwan.

- ¹A. H. C. Neto, F. Guinea, N. M. R. Peres, K. S. Novoselov, and A. K. Geim, *Rev. Mod. Phys.* **81**, 109 (2009).
- ²A. K. Geim and S. K. Novoselov, *Nat. Mater.* **6**, 183 (2007).
- ³F. Bonaccorso, Z. Sun, T. Hasan, and A. C. Ferrari, *Nat. Photonics* **4**, 611 (2010).
- ⁴Y. Shao, J. Wang, H. Hu, J. Liu, I. A. Aksay, and Y. Lin, *Electroanalysis* **22**, 1027 (2010).
- ⁵W. de Heer, C. Berger, X. Xu, P. First, E. Conrad, X. B. Li, T. Li, M. Sprinkle, J. Hass, M. L. Sadowski *et al.*, *Solid State Commun.* **143**, 92 (2007).
- ⁶K. V. Emtsev, A. Bostwick, K. Horn, J. Jobst, G. L. Kellogg, L. Ley, J. McChesney, T. Ohta, S. Reshanov, J. Rohrl *et al.*, *Nat. Mater.* **8**, 203 (2009).
- ⁷X. Li, W. Cai, J. An, S. Kim, J. Nah, D. Yang, R. Pinter, A. Velamakanni, I. Jung, E. Tutuc *et al.*, *Science* **324**, 1312 (2009).
- ⁸A. Reina, X. Jia, J. Ho, D. Nezich, H. Son, V. Bulovic, M. S. Dresselhaus, and J. Kong, *Nano Lett.* **9**, 30 (2009).
- ⁹K. S. Kim, Y. Zhao, H. Jang, S. Y. Lee, J. M. Kim, K. S. Kim, J.-H. Ahn, P. Kim, J.-Y. Choi, and B. H. Hong, *Nature* **457**, 706 (2009).
- ¹⁰T. Ando, *J. Phys. Soc. Jpn.* **74**, 777 (2005).
- ¹¹E. McCann, K. Kechedzhi, V. I. Fal'ko, H. Suzuura, T. Ando, and B. L. Altshuler, *Phys. Rev. Lett.* **97**, 146805 (2006).
- ¹²X.-Z. Yan and C. S. Ting, *Phys. Rev. Lett.* **101**, 126801 (2008).
- ¹³S. Das Sarma, S. Adam, E. H. Hwang, and E. Rossi, *Rev. Mod. Phys.* **83**, 407 (2011).
- ¹⁴E. H. Hwang and S. Das Sarma, *Phys. Rev. B* **75**, 205418 (2007).
- ¹⁵S. Adam, E. H. Hwang, V. M. Galitski, and S. Das Sarma, *Proc. Natl. Acad. Sci. U.S.A.* **104**, 18392 (2007).
- ¹⁶Q. Li, E. H. Hwang, and S. Das Sarma, *Phys. Rev. B* **84**, 115442 (2011).
- ¹⁷F. V. Tikhonenko, A. A. Kozikov, A. K. Savchenko, and R. V. Gorbachev, *Phys. Rev. Lett.* **103**, 226801 (2009).
- ¹⁸Y. F. Chen, M. H. Bae, C. Chialvo, T. Dirks, A. Bezryadin, and N. Mason, *J. Phys.: Condens. Matter* **22**, 205301 (2010).
- ¹⁹D.-K. Ki, D. Jeong, J.-H. Choi, H.-J. Lee, and K.-S. Park, *Phys. Rev. B* **78**, 125409 (2008).
- ²⁰F. V. Tikhonenko, D. W. Horsell, R. V. Gorbachev, and A. K. Savchenko, *Phys. Rev. Lett.* **100**, 056802 (2008).
- ²¹H. Cao, Q. Yu, L. A. Jauregui, J. Tian, W. Wu, Z. Liu, R. Jalilian, D. K. Benjamin, Z. Jiang, J. Bao *et al.*, *Appl. Phys. Lett.* **96**, 122106 (2010).
- ²²A. M. R. Baker, J. A. Alexander-Webber, T. Altbauer, T. J. B. M. Janssen, A. Tzalenchuk, S. Lara-Avila, S. Kubatkin, R. Yakimova, C.-T. Lin, L.-J. Li *et al.*, *Phys. Rev. B* **86**, 235441 (2012).
- ²³C. C. Tang, M. Y. Li, L. J. Li, C. C. Chi, and J. C. Chen, *Appl. Phys. Lett.* **99**, 112107 (2011).
- ²⁴A. C. Ferrari, J. C. Meyer, V. Scardaci, C. Casiraghi, M. Lazzeri, F. Mauri, S. Piscanec, D. Jiang, K. S. Novoselov, S. Roth *et al.*, *Phys. Rev. Lett.* **97**, 187401 (2006).
- ²⁵C. Casiraghi, S. Pisana, K. S. Novoselov, A. K. Geim, and A. C. Ferrari, *Appl. Phys. Lett.* **91**, 233108 (2007).
- ²⁶S. K. Novoselov, A. K. Geim, S. V. Morozov, D. Jiang, M. I. Katsnelson, I. V. Grigorieva, S. V. Dubonos, and A. A. Firsov, *Nature* **438**, 197 (2005).
- ²⁷C. Yanik and I. Kaya, *Solid State Commun.* **160**, 47 (2013).
- ²⁸X.-Z. Yan and C. S. Ting, *Phys. Rev. B* **80**, 155423 (2009).
- ²⁹X.-Z. Yan and C. S. Ting, *New J. Phys.* **11**, 093026 (2009).
- ³⁰Y.-W. Tan, Y. Zhang, H. L. Stormer, and P. Kim, *Eur. Phys. J. Spec. Top.* **148**, 15 (2007).
- ³¹K. I. Bolotin, K. J. Sikes, J. Hone, H. L. Stormer, and P. Kim, *Phys. Rev. Lett.* **101**, 096802 (2008).
- ³²Q. Li, E. H. Hwang, E. Rossi, and S. Das Sarma, *Phys. Rev. Lett.* **107**, 156601 (2011).
- ³³J. Heo, H. J. Chung, S.-H. Lee, H. Yang, D. H. Seo, J. K. Shin, U.-I. Chung, S. Seo, E. H. Hwang, and S. Das Sarma, *Phys. Rev. B* **84**, 035421 (2011).
- ³⁴J.-H. Chen, C. Jang, S. Xiao, M. Ishigami, and M. S. Fuhrer, *Nat. Nano* **3**, 206 (2008).
- ³⁵S. V. Morozov, K. S. Novoselov, M. I. Katsnelson, F. Schedin, D. C. Elias, J. A. Jaszczak, and A. K. Geim, *Phys. Rev. Lett.* **100**, 016602 (2008).

- ³⁶C.-Y. Su, Y. Xu, W. Zhang, J. Zhao, X. Tang, C.-H. Tsai, and L.-J. Li, [Chem. Mater.](#) **21**, 5674 (2009).
- ³⁷D. B. Farmer, R. Golizadeh-Mojarad, V. Perebeinos, Y.-M. Lin, G. S. Tulevski, J. C. Tsang, and P. Avouris, [Nano Lett.](#) **9**, 388 (2009).
- ³⁸J. Martin, N. Akerman, G. Ulbricht, T. Lohmann, J. H. Smet, K. Von Klitzing, and A. Yacoby, [Nat. Phys.](#) **4**, 144 (2008).
- ³⁹Y. Zhang, V. W. Brar, C. Girit, A. Zettl, and M. F. Crommie, [Nat. Phys.](#) **5**, 722 (2009).